

# Local structural characteristics of $\text{Sb}_2\text{Te}_3$ films studied by reverse Monte Carlo modeling

Ling Zhang<sup>1</sup> · San-Nian Song<sup>2</sup> · He Lin<sup>1</sup> · Yan Cheng<sup>2</sup> · Wei Xi<sup>2</sup> · Le Li<sup>2</sup> · Yan He<sup>1</sup> · Zhi-Tang Song<sup>2</sup>

Received: 28 August 2015 / Revised: 28 December 2015 / Accepted: 7 January 2016 / Published online: 4 February 2017  
© Shanghai Institute of Applied Physics, Chinese Academy of Sciences, Chinese Nuclear Society, Science Press China and Springer Science+Business Media Singapore 2017

**Abstract** Atomic configuration and connectivity of  $\text{Sb}_2\text{Te}_3$  thin film are investigated using high-energy X-ray diffraction and reverse Monte Carlo simulation. Atomic model details of  $\text{Sb}_2\text{Te}_3$  thin film are compared with liquid and amorphous  $\text{Sb}_2\text{Te}_3$  reported in other article. Simulations show that both Sb–Sb and Te–Te homopolar bonds are present in the models. In phase transition process, atomic configuration of the sample rearranges gradually through the forming of Sb–Te bonds and the breaking of Sb–Sb and Te–Te bonds.

**Keywords** Phase-change material · Reverse Monte Carlo · Atomic configuration

---

This work was supported by the National Natural Science Foundation of China (Nos. 51201178, U1232112 and 61376006), the Science and Technology Council of Shanghai (Nos. 13ZR1447200 and 14DZ2294900), and the National Key Basic Research Program of China (No. 2012CB825700).

---

✉ San-Nian Song  
songsannian@mail.sim.ac.cn

✉ He Lin  
linhe@sinap.ac.cn

<sup>1</sup> Shanghai Synchrotron Radiation Facility, Shanghai Institute of Applied Physics, Chinese Academy of Sciences, Shanghai 201204, China

<sup>2</sup> State Key Laboratory of Functional Materials for Informatics, Shanghai Institute of Micro-system and Information Technology, Chinese Academy of Sciences, Shanghai 200050, China

## 1 Introduction

Phase-change random access memory (PCRAM) has been hailed as the next generation nonvolatile memory to overcome scaling limitations faced by the current memory technology. Compared with memories such as flash, DRAM, and SRAM, PCRAM is of faster access time, higher overwrite cycle capability, lower cost, power consumption, and better compatibility with complementary metal oxide semiconductor technologies [1].

In PCRAM, the phase-change material has amorphous and crystalline phases with remarkably different properties, and each phase can reversibly transit to another on a nanosecond timescale [2]. Until now, most studies of phase-change material focus on chalcogenide pseudobinary compositions along the GeTe– $\text{Sb}_2\text{Te}_3$  tie line, for example,  $\text{Ge}_2\text{Sb}_2\text{Te}_5$ ,  $\text{GeSb}_2\text{Te}_4$ , and  $\text{GeSb}_4\text{Te}_7$  [1, 3–5]. Among them,  $\text{Ge}_2\text{Sb}_2\text{Te}_5$ , known as GST, is the most widely used material. GST inherits good thermal stability of GeTe material and fast phase-change ability of  $\text{Sb}_2\text{Te}_3$  material, showing overall qualified performances [6]. As an important component,  $\text{Sb}_2\text{Te}_3$  film has been considered as a candidate to replace GST film due to its rapid crystallization speed, but low crystallization temperature makes it inappropriate for PCRAM application [7–10]. Efforts have been made to improve the thermal stability of  $\text{Sb}_2\text{Te}_3$  films, and a promising solution is to dope Ti, Si, and N into the  $\text{Sb}_2\text{Te}_3$  film. The doping effects on structure and phase stability of the film have been studied by experiments and simulations [7, 9–11]. However, to better understand the crystallization characteristics of the doped  $\text{Sb}_2\text{Te}_3$  materials, atomic configuration and connectivity of  $\text{Sb}_2\text{Te}_3$  film itself need to be studied.

In this paper, we investigate the structure of  $\text{Sb}_2\text{Te}_3$  film by using high-energy X-ray diffraction and reverse Monte Carlo (RMC) technique with random and crystalline configuration for comparison study. To understand the crystallization behavior, atomic configuration and connectivity of the models are discussed and compared with other work [12].

## 2 Experimental

$\text{Sb}_2\text{Te}_3$  thin film was prepared on Si wafer at room temperature by magnetron sputtering using  $\text{Sb}_2\text{Te}_3$  alloy target. Powder sample for structural study was prepared through the following processes: (1) 1- $\mu\text{m}$   $\text{Sb}_2\text{Te}_3$  film was deposited on a rectangle glass substrate by magnetron sputtering using  $\text{Sb}_2\text{Te}_3$  alloy target; (2)  $\text{Sb}_2\text{Te}_3$  film was scratched off from the glass substrate using a spatula; and (3) powders were collected in a double-side compton film-walled aluminum tube of  $\Phi$  2 and 1 mm wall. Crystalline  $\text{Sb}_2\text{Te}_3$  (*c*- $\text{Sb}_2\text{Te}_3$ ) thin film was obtained by annealing for 3 min at 350 °C under  $\text{N}_2$  atmosphere.

X-ray diffraction (XRD) patterns were measured by Bruker D8 Advance powder diffractometer. High-energy XRD experiment at 69.5 keV photon energy was performed on Beamline BL13W1 at the Shanghai synchrotron radiation facility (SSRF), at room temperature and atmospheric pressure [13]. Data processing was carried out using the PDFgetX3 code [14]. Total scattering structure factor  $S(Q)$  was fitted by the RMCprofile code [15, 16].

## 3 Results and discussion

Figure 1 shows XRD patterns of  $\text{Sb}_2\text{Te}_3$  thin film after annealing for 3 min at 350 °C under  $\text{N}_2$  atmosphere. The crystallized  $\text{Sb}_2\text{Te}_3$  film shows R3 m rhombohedral structure, and no separate phase is observed. Each diffraction peak can be indexed according to the PDF card (JCPDS NO. 15-0874). The lattice parameters for  $\text{Sb}_2\text{Te}_3$  film were

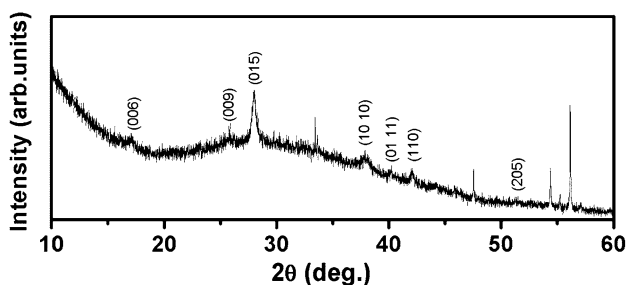


Fig. 1 XRD pattern of  $\text{Sb}_2\text{Te}_3$  thin film annealed at 350 °C

calculated to be  $a = 4.26 \text{ \AA}$  and  $c = 30.78 \text{ \AA}$ , being well consistent with previous report [17].

The RMC simulation started with a random configuration having the constraint of closest atom–atom approach to avoid physically unrealistic structure. The simulation was performed using 6000 particles with correct stoichiometry. Atomic number density is  $0.03 \text{ atoms/\AA}^3$ . Also, we started with a crystalline configuration, performed using 4860 particles with  $0.03 \text{ atoms/\AA}^3$  atomic number density, which led to similar atomic arrangement of the material phase. Throughout the RMC simulations, we carried out bond valence sums constraint, in which the type of neighbors was not constrained. The average BVS values in random and crystalline simulations were 2.774 and 2.672, respectively.

The measured structure factor  $S(Q)$  of  $\text{Sb}_2\text{Te}_3$  sample is shown in Fig. 2 (circles). The pattern is of sharper Bragg reflections than that of liquid  $\text{Sb}_2\text{Te}_3$  (*l*- $\text{Sb}_2\text{Te}_3$ ) in Ref. [12], indicating the existence of long-range periodicity in the atomic configuration. It means that part of the as-deposited  $\text{Sb}_2\text{Te}_3$  film crystallized because of its low crystallization temperature. Total structure factors  $S(Q)$  of  $\text{Sb}_2\text{Te}_3$  derived from the RMC simulations with random and crystalline models (*r*-model and *c*-model) are also shown in Fig. 2 (blue and red lines), which are consistent with the experimental data.

The bond lengths and average coordination numbers around Sb and Te atoms obtained from simulations are listed in Table 1. In order to test whether Sb–Sb and Te–Te bonds exist in the sample, the simulations were carried out with different cutoff distances. All of them showed that the existence of Sb–Sb and Te–Te bonds could lead to a good fit.

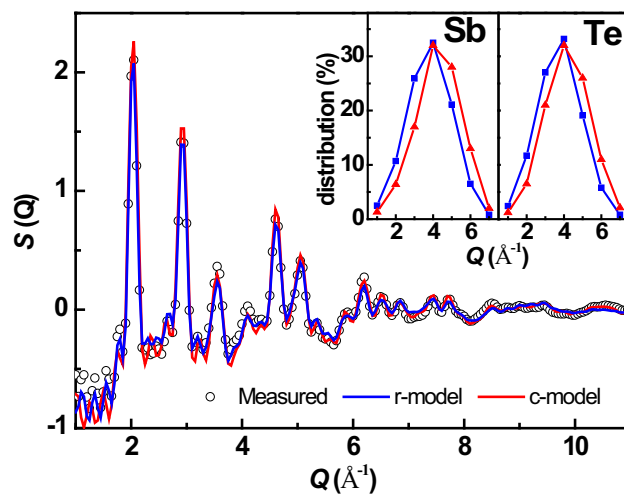


Fig. 2 Total structure factor  $S(Q)$  of  $\text{Sb}_2\text{Te}_3$ . The measured data are in circles. The blue and red lines are RMC simulated with random and crystalline configuration, respectively. The inset is distribution of coordination numbers of Sb and Te atoms derived from the RMC models. (Color figure online)

**Table 1** Bond lengths and coordination numbers in as-sputtered amorphous Sb<sub>2</sub>Te<sub>3</sub> obtained from RMC simulations

Pairs	Sb–Sb	Sb–Te	Te–Te	$N_{\text{Sb}}$	$N_{\text{Te}}$
Bond lengths (Å)	2.78	2.77	2.76	–	–
Coord. no. ( <i>r</i> -model)	1.31	3.28	2.19	4.59	4.38
Coord. no. ( <i>c</i> -model)	0.91	3.74	0.95	4.65	4.62

The *r*-model data have larger fraction of homopolar Sb–Sb and Te–Te bonds than that of the *c*-model, which is similar to the case of amorphous Sb<sub>2</sub>Te<sub>3</sub> (a-Sb<sub>2</sub>Te<sub>3</sub>) and l-Sb<sub>2</sub>Te<sub>3</sub> [12]. It can be seen that Sb atoms form bonds preferentially with Te atoms in both *r*- and *c*-model. The total coordination number around the Sb and Te atom derived from simulations is estimated at 4.59 and 4.38 for *r*-model, 4.65 and 4.62 for *c*-model, respectively. These numbers are larger than the coordination number of a-Sb<sub>2</sub>Te<sub>3</sub>, in which Sb and Te atoms are mostly four-coordinated and three-coordinated [12].

For a phase-change material, phase transition accomplishes in its heating and cooling process. The crystalline state is formed by heating the material to its crystallization temperature, but the crystalline structure is destroyed above its melting point. Strong atomic bonds or strongly localized atomic bonds need higher energy excitation to rearrange from crystalline state to amorphous state. In GST, Ge atoms locate in octahedral (crystalline) position and tetrahedral position (amorphous), [18]. In the phase-change process, transition from amorphous to crystalline can be triggered at a low energy excitation, while it takes a higher energy excitation for the structure to reorganize [6]. As an important local structural property, average coordination number represents the degree of cross-link in covalently bonded solids, which strongly affects the rigidity of atomic networks. Glassy chalcogenide materials usually have a varying covalent coordination number. It is supposed that rigid networks with more atomic linkages should be more strongly localized and more stable than less cross-linked ones. Therefore, at low temperature, the unstable a-Sb<sub>2</sub>Te<sub>3</sub> crystallizes easily to form a stable phase with larger coordination numbers. The inset in Fig. 2 shows the distribution of coordination numbers derived from two RMC models. It can be seen that in both models the total coordination number around Sb and Te is mostly 5 and 4. From Table 1 and Fig. 2, we can know that dominant short-range structural units in the models are Sb<sub>2</sub>Te<sub>3</sub> and Sb<sub>2</sub>Te<sub>4</sub>.

Silva [19] reported an increase in the average effective coordination number of crystalline phase compared with amorphous phase in both experimental and theoretical studies, and the average effective coordination numbers of Sb and Te in c-Sb<sub>2</sub>Te<sub>3</sub> were 5.89 and 4.11. In our RMC model, Te atom has a larger total coordination number,

because in our simulations, a cubic box containing fixed number of atoms is used in which fewer Te atoms locate in the border, rather than 67% of Te atoms in the border of the building blocks having coordination number of 3.17 in Ref [19].

To understand the local structure of the sample, Sb(Te)–Sb–Sb(Te) and Sb(Te)–Te–Sb(Te) bond angle distributions (BAD) are shown in Fig. 3a. In both *r*-model and *c*-model, the maximum broad peaks are centered at around 90°, indicating an octahedral local order. Another group of broad peaks is at around 60° in the two models. This is similar to the BAD in l-Sb<sub>2</sub>Te<sub>3</sub>. The peaks at around 60° are probably due to the formation of Sb–Sb and Te–Te homopolar bond (this will be further discussed later). An obvious difference between the two models is the minor peak close to 180° in the *c*-model. It indicates that some Sb(Te) atoms and their neighbors are in a linear arrangement. Detail of the BAD in Fig. 3a inset shows that most near 180° structures origin from Sb–Te–Sb and Te–Sb–Te units, which means that the Sb(Te) atoms and their neighboring atoms are in the same plane. In addition, in Fig. 3a inset the peak around 60° is rather small, suggesting that these units may possess a crystal-like bond angle order. Typical atomic configuration polyhedron of Sb with 5 coordination atoms in *r*-model is shown in Fig. 3b. The shape of SbTe<sub>5</sub> polyhedron is not a regular octahedron, which is similar to a-Sb<sub>2</sub>Te<sub>3</sub> and other disordered systems that both Sb and Te atoms are in a defective octahedral environment [12, 20].

Ring distribution is often used to analyze the medium range order in amorphous model. The ring sizes of the Sb<sub>2</sub>Te<sub>3</sub> models of up to 20-fold ring are shown in Fig. 4. In both *r*- and *c*-models, long chains are not a dominating structure. Of all the ring structures, a large percentage is small size rings, which is different from that of a-Sb<sub>2</sub>Te<sub>3</sub> [12]. In fact, 60% of the rings in the two models are three-, four- and five-membered. The *c*-model has more four- and less three-membered rings than the *r*-model. In amorphous material, maximum diameter for amorphous formation is considered as a real parameter indicating glass formation ability (GFA) of alloy. Typically, glass material with lower GFA has narrower ring distribution and is more topologically ordered [21, 22]. Therefore, it is a reasonable estimation that during amorphous–crystal process, crystallization is favored by a regular arrangement with the long chains separating to a certain size rings that gives the structure a high degree of symmetry, just as the crystallization process of a-GST and a-GeTe reported in Ref. [23].

To obtain information on partial correlations in real space, partial pair distribution functions  $g_{ij}(r)$  derived from the two RMC models are shown in Fig. 5. The covalent networks obtained in the two models are similar to each other. The  $g_{ij}(r)$  distribution for Sb–Sb and Te–Te pairs

**Fig. 3** BAD in  $\text{Sb}_2\text{Te}_3$  (a) and snapshot of typical  $\text{SbTe}_5$  defective octahedron in  $r$ -model (b). Circles line and full line represent  $c$ -model and  $r$ -model, respectively. The inset is BAD of Sb–Te–Sb and Te–Sb–Te structure in  $c$ -model

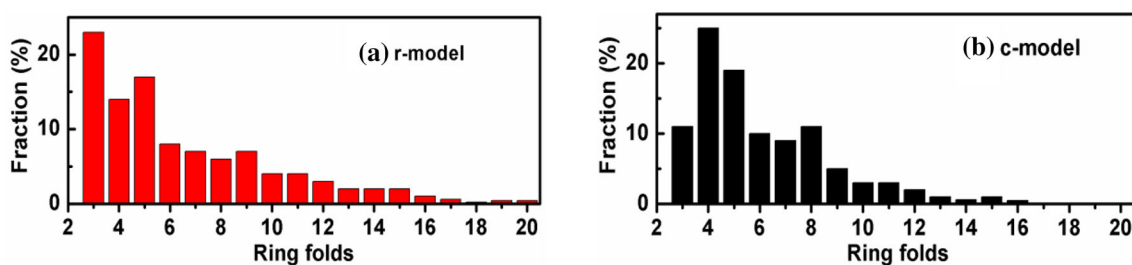
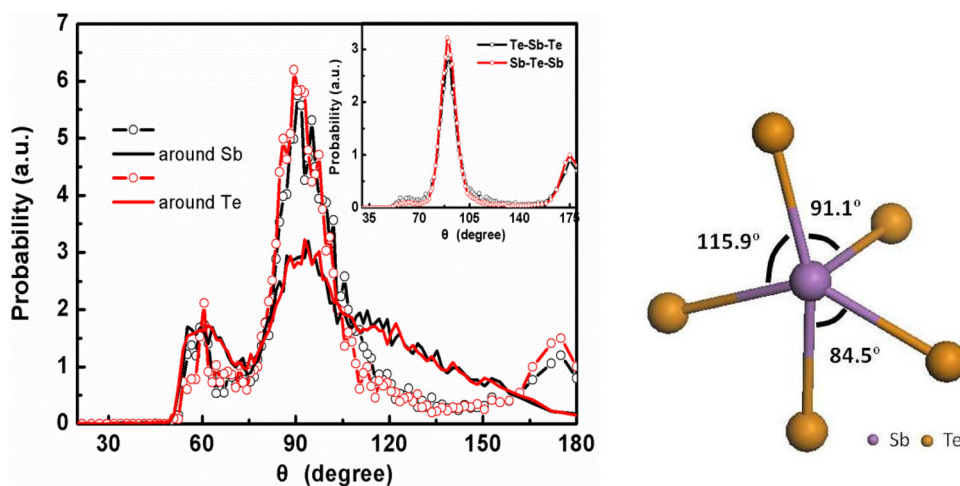


**Fig. 4** Ring size distribution in  $\text{Sb}_2\text{Te}_3$ . The ring size was counted according to the method in Ref. [12]. The ring distribution was counted from an atom in the starting point and returning to the atom

through the shortest path length, so as to avoid counting a large-number fold ring that could be divided into smaller-number fold rings

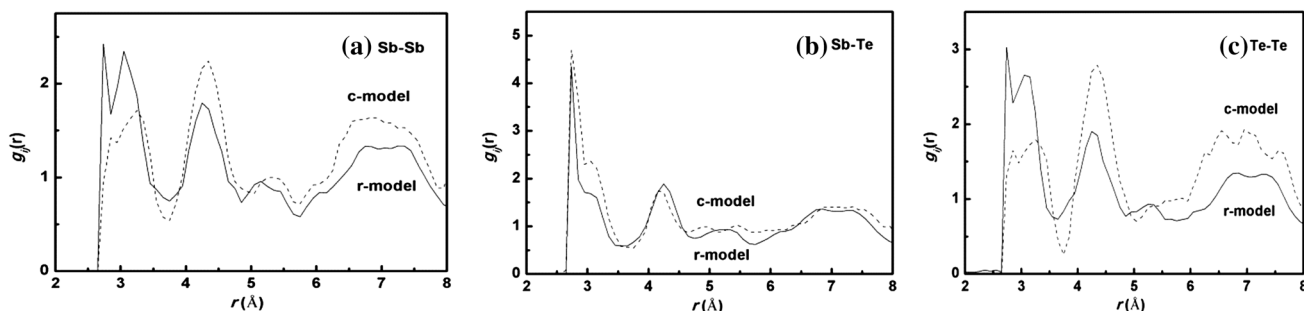


**Fig. 5** Partial pair distribution functions,  $g_{ij}(r)$ , for  $r$ -model (solid line) and  $c$ -model (dotted line) obtained from the RMC simulations

from 2.6 to 3.4 Å might attribute to the formation of Sb–Sb and Te–Te bonds in the structural units. Differences of the nearest coordination distance for Sb–Sb, Sb–Te and Te–Te pairs between the two models are not obvious. The coordination distance main peak for Sb–Sb and Te–Te pairs in  $c$ -model is longer than that of the  $r$ -model, suggesting the reduction in Sb–Sb and Te–Te coordination number in simulation.

To further explain the structure and atomic configurations, typical three- to six-membered rings in the  $r$ -model are shown schematically in Fig. 6a. In the ring distribution, about 23% is three-membered rings. Most three-membered

rings are connected with four- and five-membered rings. It is clear that the main framework of these rings consist of Sb–Te–Sb–Te bonds. Sb–Sb and Te–Te homopolar bonds mostly exist in three-membered rings.  $\text{Sb}_2\text{Te}_3$  exhibits both odd- and even- numbered rings due to the formation of Sb–Sb and Te–Te homopolar bonds. According to the structure of  $c$ - $\text{Sb}_2\text{Te}_3$ , rearrangement of the different size rings in  $a$ - $\text{Sb}_2\text{Te}_3$  is required in phase-change process. Figure 6b, c shows the probable process of the reorganization of the rings during crystallization. It may be inferred that a similar crystallization process in GeTe also occurs in  $\text{Sb}_2\text{Te}_3$  that the odd-numbered rings transform into even-numbered

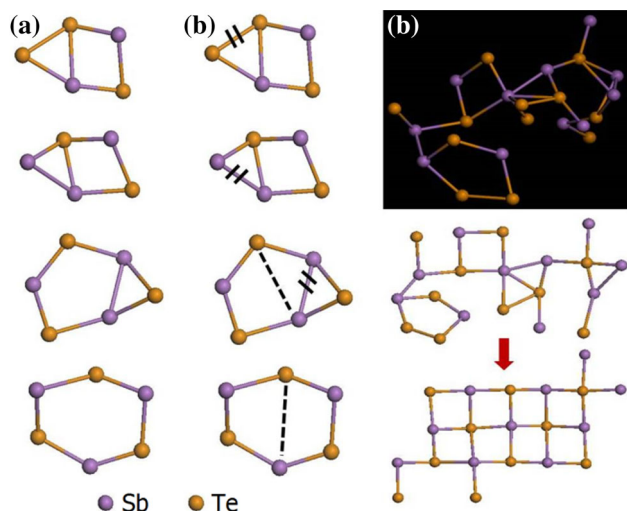


**Fig. 6** Typical three-, four-, five-, and six-membered rings in the *r*-model (a), and possible rearrangement of different rings during Sb<sub>2</sub>Te<sub>3</sub> crystallization process (b, c)

rings with the forming of Sb–Te bonds accompanied with the breaking of Sb–Sb and Te–Te bonds.

#### 4 Summary

Sb<sub>2</sub>Te<sub>3</sub> film samples have been studied using synchrotron-based X-ray diffraction and RMC simulations with random and crystalline configuration for comparison. The structure of Sb<sub>2</sub>Te<sub>3</sub> obtained by RMC modeling is presented and compared with a-Sb<sub>2</sub>Te<sub>3</sub> and l-Sb<sub>2</sub>Te<sub>3</sub> reported in references to understand the crystallization behavior of Sb<sub>2</sub>Te<sub>3</sub> thin film. Two models show similar atomic arrangement of the material phase. Based on BAD, partial pair distribution functions  $g_{ij}(r)$  and ring distribution analysis, it is found that the *c*-model exhibits a little bit more crystal-like structure than the *r*-model. The fitting results show that Sb and Te atoms are mostly fivefold and fourfold coordinated, respectively, in defective octahedral sites. Both homopolar Sb–Sb and Te–Te bonds are present in the sample. In crystallization, long chains separate to small size rings giving the structure a high degree of symmetry. It is supposed that in the amorphous–crystal process, the atomic configuration might rearrange gradually with the forming of Sb–Te bonds and breaking of Sb–Sb and Te–Te bonds.

#### References

1. L.W.W. Fang, J.S. Pan, R. Zha et al., Band alignment between amorphous Ge<sub>2</sub>Sb<sub>2</sub>Te<sub>5</sub> and prevalent complementary-metal-oxide-semiconductor materials. *Appl. Phys. Lett.* **92**, 032107 (2008). doi:10.1063/1.2837189
2. N. Yan, X.Q. Liu, L. Zhang et al., The amount of Ge tunes the atomic structure of amorphous Ge<sub>x</sub>Te<sub>1-x</sub> alloy. *Chem. Phys. Lett.* **556**, 108–112 (2013). doi:10.1016/j.cplett.2012.11.067
3. N. Yamada, E. Ohno, K. Nishiuchi et al., Rapid phase transitions of GeTeSb<sub>2</sub>Te<sub>3</sub> pseudobinary amorphous thin films for an optical disk memory. *J. Appl. Phys.* **69**, 2849–2856 (1991). doi:10.1063/1.348620
4. K. Shportko, K. Stephan, M. Woda et al., Resonant bonding in crystalline phase-change materials. *Nat. Mater.* **7**, 653–658 (2008). doi:10.1038/nmat2226
5. W. Welnic, A. Pamungkas, R. Detemple et al., Unravelling the interplay of local structure and physical properties in phase-change materials. *Nat. Mater.* **5**, 56–62 (2006). doi:10.1038/nmat1539
6. K. Ren, F. Rao, Z. Song et al., Pseudobinary Al<sub>2</sub>Te<sub>3</sub>–Sb<sub>2</sub>Te<sub>3</sub> material for high speed phase change memory application. *Appl. Phys. Lett.* **100**, 052105 (2012). doi:10.1063/1.3680580
7. M.S. Kim, S.H. Cho, S.K. Hong et al., Crystallization characteristics of nitrogen-doped Sb<sub>2</sub>Te<sub>3</sub> films for PRAM application. *Ceram. Int.* **34**, 1043–1046 (2008). doi:10.1016/j.ceramint.2007.09.078
8. M.Y. Kim, T.S. Oh et al., Crystallization behavior and thermoelectric characteristics of the electrodeposited Sb<sub>2</sub>Te<sub>3</sub> thin films. *Thin Solid Films* **518**, 6550–6553 (2010). doi:10.1016/j.tsf.2010.03.052
9. M. Zhu, L. Wu, F. Rao et al., Uniform Ti-doped Sb<sub>2</sub>Te<sub>3</sub> materials for high-speed phase change memory applications. *Appl. Phys. Lett.* **104**, 053119 (2014). doi:10.1063/1.4863430
10. X. Li, F. Rao, Z. Song et al., Experimental and theoretical study of silicon-doped Sb<sub>2</sub>Te<sub>3</sub> thin films: Structure and phase stability. *Appl. Surf. Sci.* **257**, 4566–4568 (2011). doi:10.1016/j.apsusc.2010.12.017
11. B. Qiao, J. Feng, Y. Lai et al., Phase-change memory device using Si–Sb–Te film for low power operation and multibit storage. *J. Electron. Mater.* **36**, 88–91 (2007). doi:10.1007/s11664-006-0024-1
12. S. Caravati, M. Bernasconi, M. Parrinello et al., First-principles study of liquid and amorphous Sb<sub>2</sub>Te<sub>3</sub>. *Phys. Rev. B* **81**, 014201 (2010). doi:10.1103/PhysRevB.81.014201
13. H.L. Xie, B. Deng, G.H. Du et al., Latest advances of X-ray imaging and biomedical applications beamline at SSRF. *Nucl. Sci. Tech.* **26**, 020102 (2015). doi:10.13538/j.1001-8042/nst.26.020102
14. P. Juháš, T. Davis, C.L. Farrow et al., PDFgetX3: a rapid and highly automatable program for processing powder diffraction data into total scattering pair distribution functions. *J. Appl. Cryst.* **46**, 560–566 (2013). doi:10.1107/S002188913005190
15. R.L. McGreevy, L. Pusztai, Reverse Monte Carlo simulation: a new technique for the determination of disordered structures. *Mol. Simulat.* **1**, 359–367 (1988). doi:10.1080/08927028808080958
16. M. G. Tucker, D. A. Keen, M. T. Dove, et al. RMCProfile: reverse Monte Carlo for polycrystalline materials. *J. Phys. Condens. Matter*, **19**, 335218 (16 pp) (2007). doi:10.1088/0953-8984/19/33/335218
17. C. Peng, L. Wu, Z. Song et al., Performance improvement of Sb<sub>2</sub>Te<sub>3</sub> phase change material by Al doping. *Appl. Surf. Sci.* **257**, 10667–10670 (2011). doi:10.1016/j.apsusc.2011.07.072
18. A.V. Kolobov, P. Fons, A.I. Frenkel et al., Understanding the phase-change mechanism of rewritable optical media. *Nat. Mater.* **3**, 703–708 (2004). doi:10.1038/nmat1215
19. J.L.F.D. Silva, Effective coordination concept applied for phase change (GeTe)<sub>m</sub>(Sb<sub>2</sub>Te<sub>3</sub>)<sub>n</sub> compounds. *J. Appl. Phys.* **109**, 023502 (2011). doi:10.1063/1.3533422
20. S. Caravati, M. Bernasconi, T.D. Kühne et al., Coexistence of tetrahedral- and octahedral-like sites in amorphous phase change

- materials. *Appl. Phys. Lett.* **91**, 171906 (2007). doi:[10.1063/1.2801626](https://doi.org/10.1063/1.2801626)
21. S. Kohara, J. Akola, H. Morita et al., Relationship between topological order and glass forming ability in densely packed enstatite and forsterite composition glasses. *Proc. Natl. Acad. Sci. USA* **108**, 14780–14786 (2011). doi:[10.1073/pnas.1104692108](https://doi.org/10.1073/pnas.1104692108)
22. Y.C. Kim, W.T. Kim, D.H. Kim et al., Glass forming ability and crystallization behavior in amorphous  $\text{Ti}_{50}\text{Cu}_{32-x}\text{Ni}_{15}\text{Sn}_3\text{Be}_x$  ( $x = 0,1,3,7$ ) alloys. *Mater. Trans.* **43**, 1243–1247 (2002). doi:[10.2320/matertrans.43.1243](https://doi.org/10.2320/matertrans.43.1243)
23. S. Kohara, K. Kato, S. Kimura et al., Structural basis for the fast phase change of  $\text{Ge}_2\text{Sb}_2\text{Te}_5$ : ring statistics analogy between the crystal and amorphous states. *Appl. Phys. Lett.* **89**, 201910 (2006). doi:[10.1063/1.2387870](https://doi.org/10.1063/1.2387870)